ORGANIC PROCESS RESEARCH & DEVELOPMENT
OPR&D

pubs.acs.org/OPRD

Article

A Virtual Plant for Integrated Continuous Manufacturing of a Carfilzomib Drug Substance Intermediate, Part 2: Enone Synthesis via a Barbier-Type Grignard Process

Elçin Içten,* Andrew J. Maloney, Matthew G. Beaver, Xiaoxiang Zhu, Dongying E. Shen, Jo Anna Robinson, Andrew T. Parsons, Ayman Allian, Seth Huggins, Roger Hart, Pablo Rolandi, Shawn D. Walker, and Richard D. Braatz

Cite This: *Org. Process Res. Dev.* 2020, 24, 1876–1890

Read Online

ACCESS | Metrics & More | Article Recommendations

ABSTRACT: This article details efforts to characterize and develop a process control strategy for the manufacture of enone **2**, a carfilzomib drug substance intermediate obtained through a Barbier-type Grignard reaction of morpholine amide **1**. This includes the development of a novel mechanistic model for the heterogeneous Barbier-type Grignard reaction. After the model was characterized with laboratory-scale batch experiments, its performance was compared with experimental data collected under continuous operating conditions. Under nominal operating conditions, the experimentally measured conversion of morpholine amide varied from 94.3% to 96.7%, a range that was encompassed by the model. With a mechanistic model validated under continuous operating conditions, relationships between the magnesium charging interval and the variability in conversion of morpholine amide **1** to enone **2** were determined to further explore the experimental design space. The remaining unit operations were subsequently characterized, and the models developed for the individual operations were integrated into a flowsheet-level dynamic process model implemented in the gPROMS FormulatedProducts software. The impact of various process disturbances and model uncertainties on the critical quality attributes were then investigated, and critical process parameters, failure modes, and control strategies to address these disturbances were identified. The process was found to be most sensitive to operational disturbances in the supplied reactants: morpholine amide **1** and 2-bromopropene (2-BP). As **1** is manufactured upstream by the process described in Part 1 of this series, in silico analysis of potential process control strategies focused on manipulation of the 2-BP concentration and flow rate into the primary reactor. Overall, this work highlights the benefits of using mathematical modeling to deepen the understanding of pharmaceutical manufacturing processes and enable integrated unit operations in a continuous manufacturing setting.

KEYWORDS: *continuous pharmaceutical manufacturing, process systems engineering, small-molecule API, flow chemistry, heterogeneous surface reaction, advanced process control*

1. INTRODUCTION

In recent years, academia, industry, and regulatory agencies have been advocating for a transition from batch processing to continuous manufacturing of pharmaceuticals.[1−3] As described by the U.S. Food and Drug Administration (FDA), continuous manufacturing offers several advantages over batch processes, including reduction of equipment size and footprint, consequential improvement of heat and mass transfer that can make possible the implementation of highly exothermic and diffusion-limited heterogeneous reactions, and the ability to divert material in cases of detected process failure.[3] Academically and industrially, there have been various demonstrations of continuous processing for individual unit operations and a limited number of demonstrations of end-to-end continuous processes, as discussed in Part 1 of this series (10.1021/acs.oprd.0c00187).[4] However, along with the advantages come some unique challenges for continuous manufacturing. Specifically, continuous processing results in more direct and complex interactions among the series of integrated unit operations. To avoid the need for an exponentially large number of experiments to characterize these potential interactions, a systems approach for process design, control, and optimization is typically adopted.[3,5−8] This systems approach involves development and validation of first-principles models for each unit operation in isolation and subsequent integration of these isolated models under one common framework. This integrated model can then be used to evaluate the impact of various process disturbances on the process dynamics and performance, enabling the determination of critical process parameters (CPPs) for each critical quality attribute (CQA). In addition, the ability to simulate the

Special Issue: Flow Chemistry Enabling Efficient Synthesis

Received: April 15, 2020
Published: July 14, 2020

end-to-end process dynamics with an integrated model allows for a systematic material- and time-sparing approach to create a process control strategy that ensures high-quality products. Similar approaches have been demonstrated in academia for the continuous drug substance manufacturing process of aliskiren hemifumarate[9−11] as well as traditional[1,12] and innovative[13,14] continuous drug product processes. Having adopted a model-based systems approach to develop control strategies, our work for a carfilzomib drug substance intermediate continues to advance the future of pharmaceutical manufacturing that ensures the supply of quality product through the use of control strategies based on advanced process modeling.[15]

Part 1 of this series introduces the end-to-end continuous process to prepare an epoxy ketone intermediate used for the manufacture of carfilzomib via a four-step synthetic sequence.[4] Part 1 also focuses on the development of a continuous manufacturing process to produce the first isolated product, morpholine amide **1**, from Boc-D-leucine monohydrate and introduces the methodology of using a virtual plant for in silico disturbance analysis and control strategy development.

Part 2 of this series describes the development of a continuous Barbier-type Grignard process to produce enone **2** from morpholine amide **1** (Scheme 1). The challenges

Scheme 1. Conversion of Morpholine Amide 1 to Enone 2 via a Mg-Mediated Barbier-Type Grignard Reaction with 2-Bromopropene

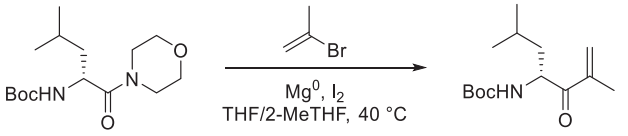

morpholine amide **1** enone **2**

associated with industrial-scale implementation of Grignard processes are well-documented and include (1) the large exotherms associated with these processes, (2) the difficulty of developing robust initiation protocols for the formation of Grignard reagents, and (3) the sensitivity of Grignard reagents to air and water, which complicates storage and shipping.[16−19] To address the aforementioned challenges, the Grignard process described herein adopts (1) a continuous approach that improves the heat and mass transfer through improved surface area to volume ratios and (2) a Barbier reaction that forms the Grignard reagent in situ in the presence of an alkenyl bromide such that the reagent is consumed upon its formation.[17,19]

Here we present a new kinetic model to describe the generation of the Grignard reagent from 2-bromopropene (2-BP) and magnesium. Others have modeled similar Grignard chemistry.[20] The kinetic model assumes that the Grignard reaction occurs by diffusion of 2-BP from the bulk phase through a mass transfer boundary layer to react on the Mg surface. The model was fit to experimental data and used (1) to develop relationships between the Mg charging interval and reactor performance and (2) to determine the impact of process disturbances on the integrated process performance, including the conversion of morpholine amide **1** to enone **2**, a critical in-process control. It is found that (1) the continuously stirred tank reactor (CSTR) performance can be maintained at a Mg charging interval of approximately 1 h and (2) the existing process configuration and operation strategy are sensitive to disturbances in the flow rates and concentrations of the morpholine amide and 2-BP feeds, with a deviation of 10% in any one of these reaction conditions leading to a reaction conversion lower than the targeted 95%.

2. VIRTUAL PLANT DEVELOPMENT FOR ENONE SYNTHESIS

The reaction to generate enone **2** consists of multiple elementary steps followed by liquid−liquid separation operations; the chemical scheme is depicted in Scheme 2, and the process flow diagram for continuous operation is shown in Scheme 3. This process involves feeding a stream of morpholine amide **1** and a solution of 2-BP into CSTR1 along with portionwise solid dosing of Mg turnings to generate the Grignard reagent, isopropenylmagnesium bromide. The liquid effluent of CSTR1 is sent to CSTR2 for additional residence time, and Mg turnings are retained in CSTR1 through the use of a Mg trap.[21] In both CSTRs, the Grignard reagent reacts with morpholine amide **1** to form deprotonated morpholine amide **3** and tetrahedral intermediate **4**, which is subsequently converted to enone **2** in CSTR3 upon protonation with citric acid. The potential CPPs that impact the CQAs of this process include (1) the feed rates of morpholine amide **1** and 2-BP, (2) the agitation rate for CSTR1 containing a heterogeneous mixture, (3) the temperatures across all of the CSTRs, (4) the mean residence time for all of the CSTRs, and (5) the schedule for charging of Mg to CSTR1. These parameters must be chosen such that the desired reaction yield is achieved with guaranteed process safety and maximized process efficiency.

The organic phase of the liquid stream from CSTR3 is separated from its aqueous phase in DEC1 and sent to CSTR4, where it is washed with 8 wt % sodium bicarbonate ($NaHCO_3$) to remove residual citric acid in the organic stream. Next, the organic phase of the liquid stream from CSTR4 is again separated from its aqueous phase in DEC2 and collected in a hold tank. After the hold tank reaches a specified volume, a fixed volume of liquid from the hold tank is sent to the batch distillation drum and distilled to a specified volume. To that distilled volume is added a fixed volume of acetonitrile (ACN), and the resulting mixture is distilled once more to a

Scheme 2. Chemical Synthesis of Enone 2

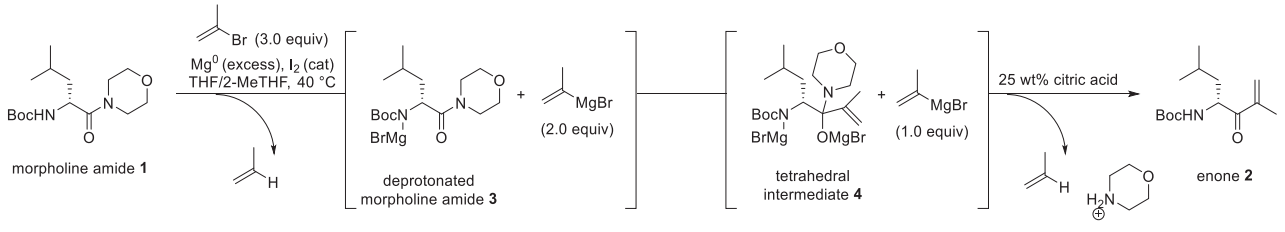

https://dx.doi.org/10.1021/acs.oprd.0c00188
Org. Process Res. Dev. 2020, 24, 1876−1890

Scheme 3. Process Flow Diagram for the Continuous Process That Converts Morpholine Amide 1 to Enone 2

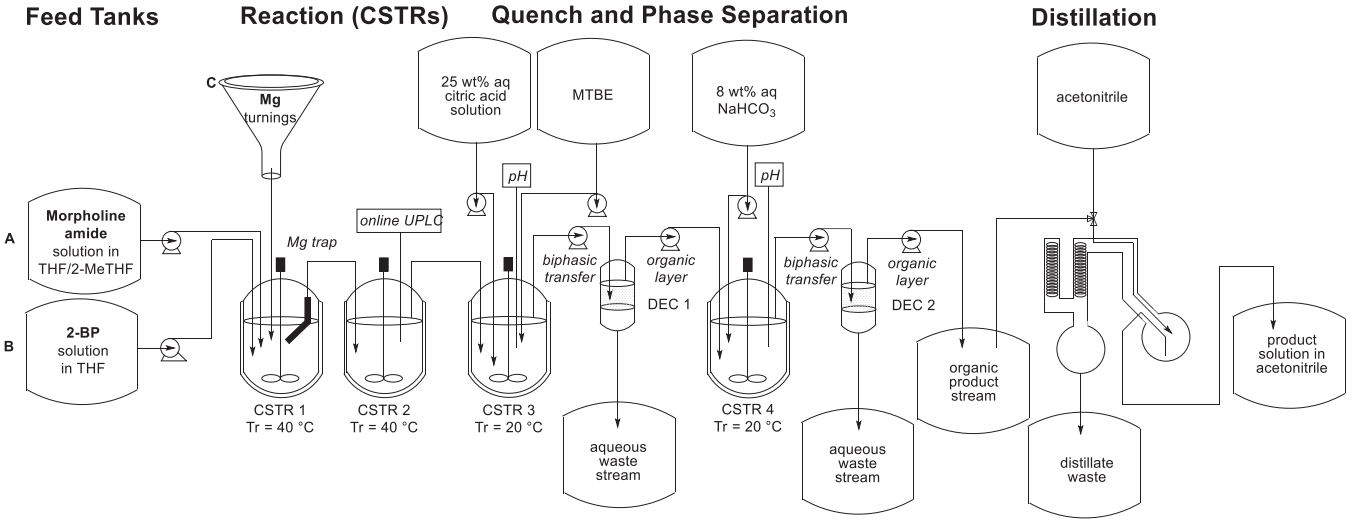

final volume. The concentrated solution of enone in ACN is collected in another hold tank, diluted with acetic acid, and sent downstream for further synthesis and purification steps as described in Part 3 of this series (10.1021/acs.oprd.0c00189).[22] The automated batch distillation operation allows for integration of continuous upstream and downstream unit operations to build an end-to-end process.

2.1. Barbier-Type Grignard Reaction Kinetic Model Derivation and Development. A complex set of biphasic reactions occurs in CSTR1. The first reaction, formation of the Grignard reagent, involves the reaction of solid Mg and liquid 2-BP to form isopropenylmagnesium bromide (eq 1).

$$\text{Mg} + \text{2-BP} \rightarrow \text{isopropenyl-MgBr} \tag{1}$$

This reaction occurs only in CSTR1.

Here we propose a new mathematical model to describe the Grignard formation mechanism wherein the reaction occurs by diffusion of 2-BP to the surface of Mg particles. A model for similar chemistry in which Mg particles are assumed to diffuse from the magnesium surface to react with 2-BP has been previously reported.[20] While this formulation can describe experimental observations, the extremely low solubility of solid Mg in tetrahydrofuran (THF) and 2-methyltetrahydrofuran (MeTHF) makes bulk diffusion of Mg an unlikely mechanism. In the proposed mechanism, the time dependence of the bulk concentration of 2-BP (C_{2BP}) is described by the mass transfer coefficient (k_L), the volumetric surface area available for diffusion of 2-BP to Mg particles (a), and the concentration of 2-BP at the surface of Mg particles (C^*_{2BP}):

$$\frac{dC_{2BP}}{dt} = -k_L a(C_{2BP} - C^*_{2BP}) \tag{2}$$

The rate of the surface reaction between Mg and 2-BP depends on the reaction rate constant (k_r), the surface concentration of 2-BP, and the surface concentration of Mg (C^*_{Mg}):

$$r_{Grignard} = k_r a C^*_{Mg} C^*_{2BP} \tag{3}$$

The reaction rate constant k_r follows an Arrhenius temperature dependence:

$$k_r = k \exp\left[-\frac{E_a}{R}\left(\frac{1}{T} - \frac{1}{T_{ref}}\right)\right] \tag{4}$$

where k is the pre-exponential factor for the reaction, E_a is the activation energy, R is the universal gas constant, T_{ref} is the reference temperature, and T is the temperature at which the rate constant is to be determined.

Under the assumption that there is no accumulation of 2-BP on the surface of the Mg particles, the rate of removal of 2-BP is equal to the rate of the surface reaction between Mg and 2-BP:

$$k_L a(C_{2BP} - C^*_{2BP}) = k_r a C^*_{Mg} C^*_{2BP} \tag{5}$$

Equations 2 and 5 can be simplified to remove the dependence on C^*_{2BP}, the surface concentration of 2-BP:

$$\frac{dC_{2BP}}{dt} = -r_{Grignard} = -\frac{k_L k_r C^*_{Mg} a}{k_L + k_r C^*_{Mg}} C_{2BP} \tag{6}$$

The volumetric surface area a can be approximated by correlating the mass of solid Mg at time t ($Mg_s(t)$) to its initial mass ($Mg_s(0)$):

$$a = a_{Mg}(0)\left[\frac{Mg_s(t)}{Mg_s(0)}\right]^{2/3} \tag{7}$$

where $a_{Mg}(0)$ is the initial volumetric surface area of Mg particles, which are assumed to be monodispersed spheres. Substitution of eq 7 into eq 6 gives

$$\frac{dC_{2BP}}{dt} = -\frac{k_L k_r C^*_{Mg}}{k_L + k_r C^*_{Mg}} a_{Mg}(0)\left[\frac{Mg_s(t)}{Mg_s(0)}\right]^{2/3} C_{2BP} \tag{8}$$

The time-dependent mass of Mg can be tracked through the stoichiometry of the Grignard reaction, the rate of the Grignard reaction ($r_{Grignard}$), the molecular weight of Mg (MW_{Mg}), and the total reaction volume (V):

$$\frac{dMg_s}{dt} = -MW_{Mg} V r_{Grignard} \tag{9}$$

https://dx.doi.org/10.1021/acs.oprd.0c00188
Org. Process Res. Dev. 2020, 24, 1876−1890

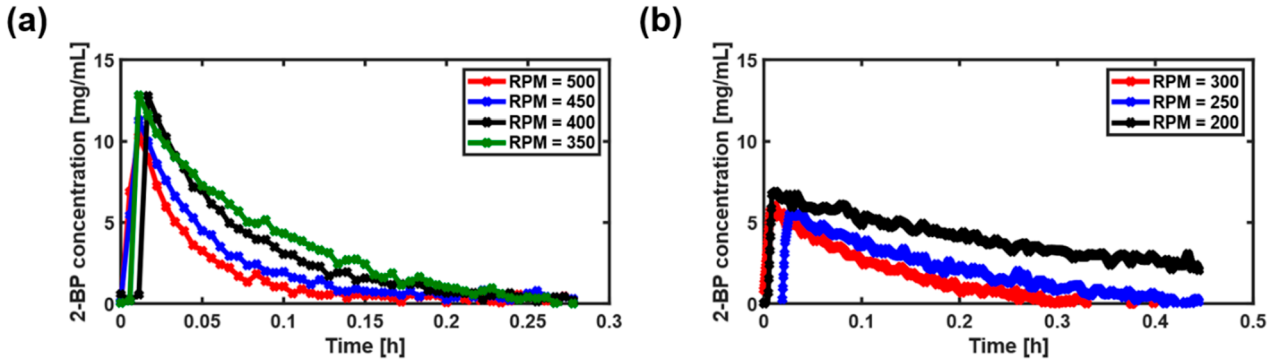

Figure 1. Concentration of 2-BP during the Grignard reaction at 40 °C and various agitation speeds: (a) 350−500 rpm; (b) 200−300 rpm.

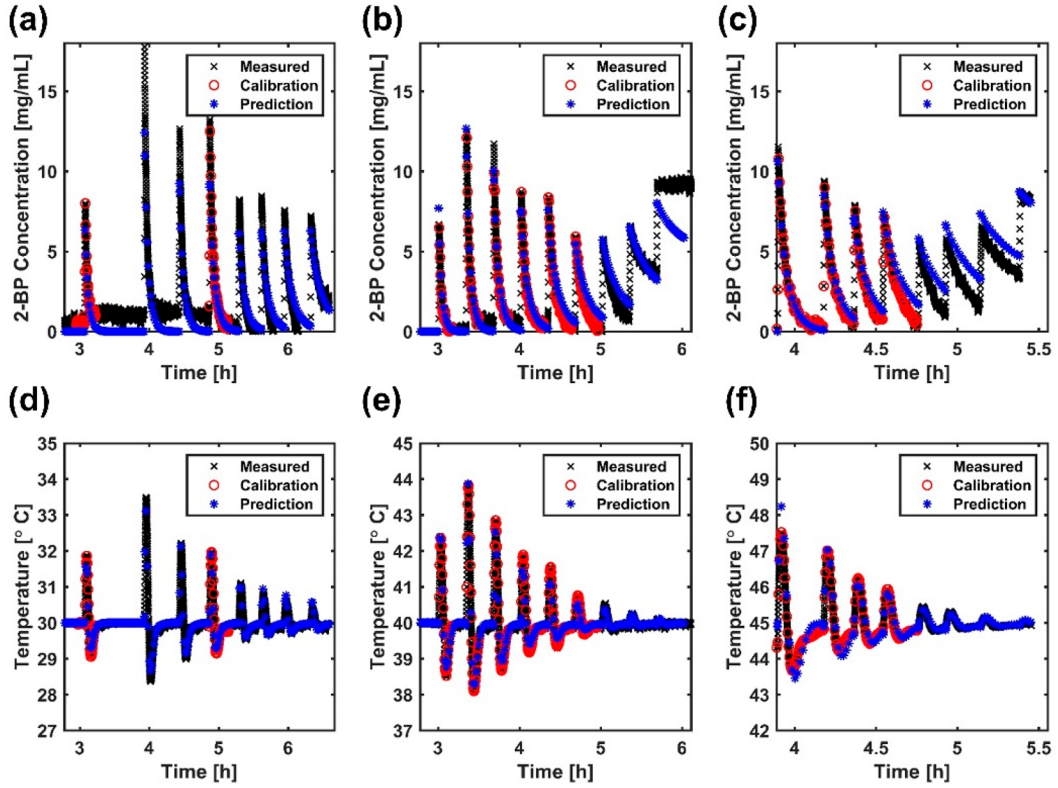

Figure 2. Comparison between model predictions and experimental values for (a−c) the 2-BP concentration and (d−f) the reactor temperature at (a, d) 30 °C, (b, e) 40 °C, and (c, f) 45 °C.

If the reaction is kinetically limited rather than mass-transfer-limited (i.e., $k_L \gg k_r C^*_{Mg}$), the total reaction rate constant can be reduced to a lumped surface reaction rate:

$$\frac{k_L k_r C^*_{Mg}}{k_L + k_r C^*_{Mg}} \approx k_r C^*_{Mg} \tag{10}$$

This assumption, which is key to model simplification, was validated experimentally. Reactions at various agitation levels (500 to 200 rpm in 50 rpm increments) were performed in 100 mL reactors with overhead agitation. At each agitation level, the 2-BP disappearance rate was recorded through Fourier transform infrared spectroscopy (FTIR) to identify the just-suspended agitation speed (N_{js}), at which the reaction overcomes mass transfer limitations. This was accomplished in a single reaction vessel with Mg in excess; each data set corresponds to a single addition of 2-BP followed by an agitation reduction of 50 rpm (Figure 1). Upon analysis of the varying 2-BP consumption rates, N_{js} was determined to be 350 rpm, and the process was then designed to be operated at ≥500 rpm, which is well above N_{js}.

A set of batch kinetic experiments were then designed and executed to validate the mechanistic model for the Grignard generation. The volumetric scale of experiments was 60 to 90 mL of total reaction mixture, and time series data of vessel temperature and 2-BP concentration were collected. To begin the experiment, solid Mg was activated by the I_2 method reported previously.[19] Following activation of solid Mg, 2-BP was added in boluses to the reaction mixture until the solid Mg was depleted. This design allowed the molar ratio of Mg in solution to 2-BP in the bolus (the Mg to 2-BP ratio) to be varied from 11 to 0.5, thus characterizing a wider range of Mg

https://dx.doi.org/10.1021/acs.oprd.0c00188
Org. Process Res. Dev. 2020, 24, 1876−1890

to 2-BP ratios than the targeted ratio of 3 in continuous operation. The reaction temperature was varied between 35 and 45 °C, with the agitation rate kept constant at 500 rpm (Figure 2). The model was calibrated at higher Mg to 2-BP ratios (red circles in Figure 2), as they are more relevant to continuous operation. Moreover, the greatest disagreement between the measured data and the model predictions occurs at the end of the run, where both the Mg to 2-BP ratio is quite low and experimental errors (i.e., discrepancies in charged Mg or 2-BP) have accumulated.

As mentioned, Grignard reactions are generally exothermic, with the heat of reaction for the chemical reaction described by eq 1 measured to be 304.1 kJ/mol of 2-BP. As shown in Figure 2, this exothermic activity results in temperature oscillations of up to 4 °C above the set point during the batch runs. To address this variability, heat transfer within the reactor was modeled with gPROMS FormulatedProducts embedded equations for temperature controllers and reaction vessels, and the overall heat transfer coefficient (UA) and the process time for the temperature controller (τ) were regressed with the supplied temperature data (Table 1). The final parameter in this model, the initial volumetric surface area of Mg turnings, $a_{Mg}(0)$, was measured experimentally as 22 420.2 m^2/m^3 using a Micromeritics TriStar II surface area analyzer.

Table 1. Regressed Kinetic Parameters of the Grignard Reaction for the Surface Reaction Rate Expression and Reactor Heat Transfer Model (T_{ref} = 40 °C) Along with 95% Confidence Intervals and Measured Initial Volumetric Surface Area of Mg Turnings

parameter	value	units
$k_r C^*_{Mg}$	$6.59 \times 10^{-6} \pm 4.37 \times 10^{-8}$	m/s
E_a	13.56 ± 0.89	kJ/mol
UA	$1.13 \pm (0.90 \times 10^{-2})$	W/°C
τ	43.37 ± 0.48	S
$a_{Mg}(0)$	22.40×10^3	m^2/m^3

The conversion of morpholine amide, a CQA for this process, occurs via deprotonation of the morpholine amide and formation of the tetrahedral intermediate (and propene) by reaction with the newly formed Grignard reagent (Scheme 2, vide supra). These two reactions, which occur in both CSTR1 and CSTR2, are described in eqs 11 and 12:

morpholine amide + isopropenyl-MgBr
→ deprotonated morpholine amide + propene (11)

deprotonated morpholine amide + 2 isopropenyl-MgBr
→ tetrahedral intermediate (12)

The heat of reaction for the combined two reactions was measured to be 271.08 kJ/mol of morpholine amide, increasing the adiabatic temperature rise of the combined Grignard formation, deprotonation, and nucleophilic addition reactions to 203 °C. These are the key reactions that occur in CSTR1 and CSTR2—no other major impurities were identified during process characterization, and 85% mass recovery was demonstrated at the batch scale.

In theory, only a total of 2 equiv of isopropenylmagnesium bromide is required for the process to occur; in practice, however, 3 equiv of isopropenylmagnesium bromide was required to achieve high conversion of morpholine amide to the tetrahedral intermediate in replicate experiments. The first elementary step is deprotonation of the carbamate of the morpholine amide (MA) with 1 equiv of isopropenylmagnesium bromide to form the deprotonated species **3**. The stoichiometric requirements of the second elementary step, nucleophilic addition to the deprotonated species, may be impacted by a complex higher-order agglomerate network of either the deprotonated species itself or the Grignard reagent as governed by the Schlenk equilibrium.[23]

The reaction rate equations are described by eqs 13 and 14:

$$r_2 = k_2 C_{Grignard} C_{MA} \quad (13)$$

$$r_3 = k_3 C_{Grignard} C_{deprotonated\ MA} \quad (14)$$

where k_2 and k_3 follow an Arrhenius-type temperature dependence a shown in eq 4. In eq 14, the dependence of the rate on the concentration of the Grignard reagent is assumed to be first-order because only one species, i.e. the dimer, is required to interact with deprotonated morpholine amide **1**.

To characterize these reactions, a set of batch kinetic experiments were designed and executed. For this, the reaction temperature was varied between 30 and 40 °C, and the molar ratio of 2-BP to morpholine amide was kept at 3. The volumetric scale was 60 to 90 mL of total reaction mixture for these experiments. Time series data were collected to track the depletion of the morpholine amide and the formation of the tetrahedral intermediate via high-performance liquid chromatography (HPLC). Figure 3 shows the experimental data and model fit, and the fitted model parameters are listed in Table 2.

After being calibrated with batch experiments, the kinetic model for the Barbier-type Grignard reaction was validated in continuous operation. The first set of experiments evaluated

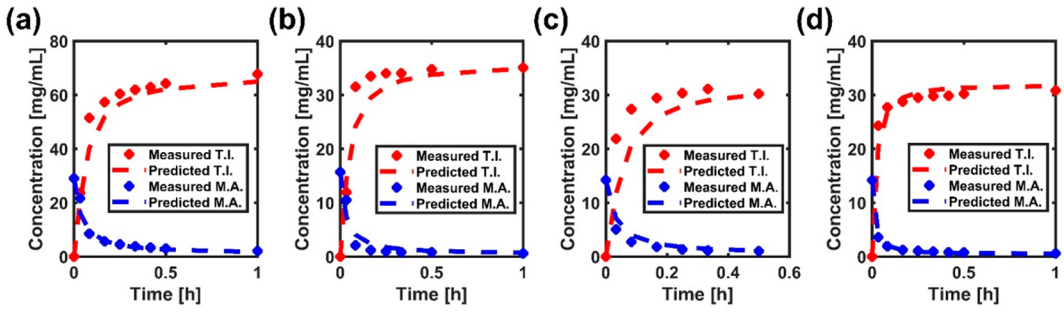

Figure 3. Comparison between model predictions and experimental values for morpholine amide (M. A.) consumption and tetrahedral intermediate (T. I) production at (a) 30 °C, (b, c) 35 °C, and (d) 40 °C.

https://dx.doi.org/10.1021/acs.oprd.0c00188
Org. Process Res. Dev. 2020, 24, 1876−1890

Table 2. Regressed Kinetic Parameters of Equations 13 and 14 to Produce the Tetrahedral Intermediate Shown with 95% Confidence Intervals (T_{ref} = 40 °C)

parameter	value	units
k_2	$1.37 \times 10^{-4} \pm 1.89 \times 10^{-5}$	$m^3\ mol^{-1}\ s^{-1}$
E_{a2}	142.97 ± 17.3	kJ/mol
k_3	$4.63 \times 10^{-4} \pm 2.37 \times 10^{-4}$	$m^3\ mol^{-1}\ s^{-1}$
E_{a3}	128.26 ± 65.3	kJ/mol

the impact of the residence time on the overall conversion of morpholine amide (Figure 4). At a Mg dosing interval of 50 min, an individual reactor volume of 100 mL, and a reactor temperature at 45 ± 5 °C, the residence time for each reactor was varied from 13 to 40 min. Figure 4 shows that the maximum disagreement between the model-predicted conversion and the experimental measurements is below 4.3%. Figure 4 also demonstrates the relationship between the dosing interval, reactor residence time, and variability in morpholine amide conversion. For the shortest residence time of 13 min (condition 3 in Figure 4), both the model-predicted and experimentally measured morpholine amide conversion ranges are the highest among the conditions studied. These variabilities result from the semibatch (i.e., noncontinuous) additions of magnesium. Accordingly, as the ratio of the dosing interval to the reactor residence time increases, so does the range of magnesium concentrations in the reactor and the morpholine conversion variability. While the model results are acceptable, the impact of the residence time on the morpholine amide conversion is underpredicted. The model is most accurate at the residence time of 40 min and has greater prediction error at the lower residence times.

Following regression, the model was further validated for extended operation. Two cases were studied: (1) a 40 min Mg dosing interval with a 20 min residence time per reactor at 40 °C and (2) a 30 min Mg dosing interval with a 30 min residence time per reactor at 30 °C. The reactions were initiated with a mixture of magnesium, 2-BP, and morpholine amide in a smaller working volume, an approximately 500 mL batch for case (1) and an approximately 200 mL batch for case (2). The mixture was aged overnight, after which continuous operation began; the zero-time point refers to the end of overnight aging. As shown in Figure 5, the model-predicted conversion of morpholine amide for case (1) matches the corresponding experimental measurement, whereas that for case (2) deviates more from the experimental measurement. The experimental data for these two case studies, summarized in Table 3, also demonstrate significant variability in the conversion of morpholine amide, indicating the importance of disturbance analysis to evaluate the process robustness toward fluctuations in the operating conditions. Finally, better agreement between the model and data and a greater overall morpholine amide conversion were observed in case (1). Therefore, the rest of this paper considers these conditions.

The validated range for this model is as follows: reactor temperature of 30−40 °C, residence time of 10−40 min, dosing interval of 30−50 min, and 12−24 equiv of residual magnesium. The model tends be more accurate at greater residence times and greater magnesium dosing intervals. The model can account for decreased residence time at large residual magnesium levels, but mass transfer limitations beyond the validated range have not been investigated and may impact the predictive power.

2.2. Workup Steps: Reaction Kinetics, Liquid−Liquid Extraction, Mass Transfer, and Model Development. The reaction kinetic formulation for the aqueous workup includes two reactions in CSTR3: (1) the reaction of the tetrahedral intermediate (TI) with citric acid to form the enone (the desired product), morpholine citrate, and magnesium bromide citrate (eq 15) and (2) the reaction of isopropenylmagnesium bromide with citric acid to form magnesium bromide citrate and propene (eq 16):

$$3\ \text{citric acid} + \text{TI} \rightarrow \text{enone} + \text{morpholine citrate} + 2\text{MgBr}\cdot\text{citrate} \quad (15)$$

$$\text{citric acid} + \text{isopropenyl-MgBr} \rightarrow \text{MgBr}\cdot\text{citrate} + \text{propene} \quad (16)$$

Both reactions were confirmed to be fast under acidic reaction conditions, reaching complete conversion in less than 1 min. Further optimization of the residence time was not needed because the reaction was instantaneous relative to the residence time of 10 min defined in CSTR3. The reactions were then assigned arbitrarily high rate constants to ensure high conversion in the gPROMS FormulatedProduct-based model.

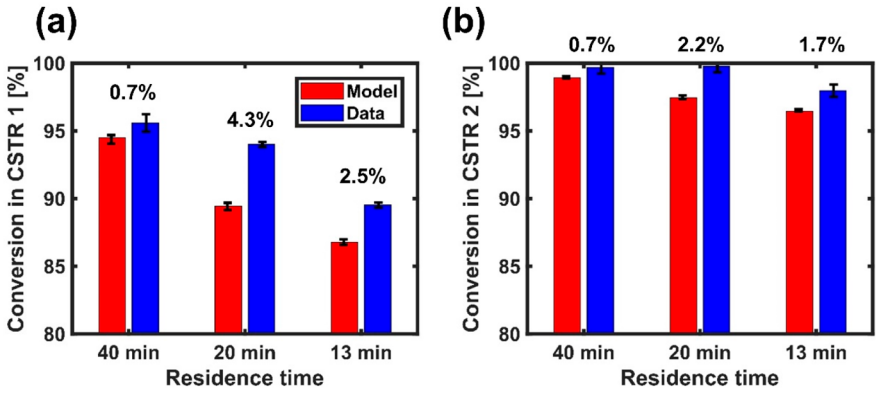

Figure 4. Comparison between model predictions and experimental values for conversion of morpholine amide in (a) CSTR1 and (b) CSTR2 at residence times of (1) 40 min per reactor, (2) 20 min per reactor, and (3) 13 min per reactor. Above each set of data is shown the difference between the model prediction and the experimental data.

https://dx.doi.org/10.1021/acs.oprd.0c00188
Org. Process Res. Dev. 2020, 24, 1876−1890

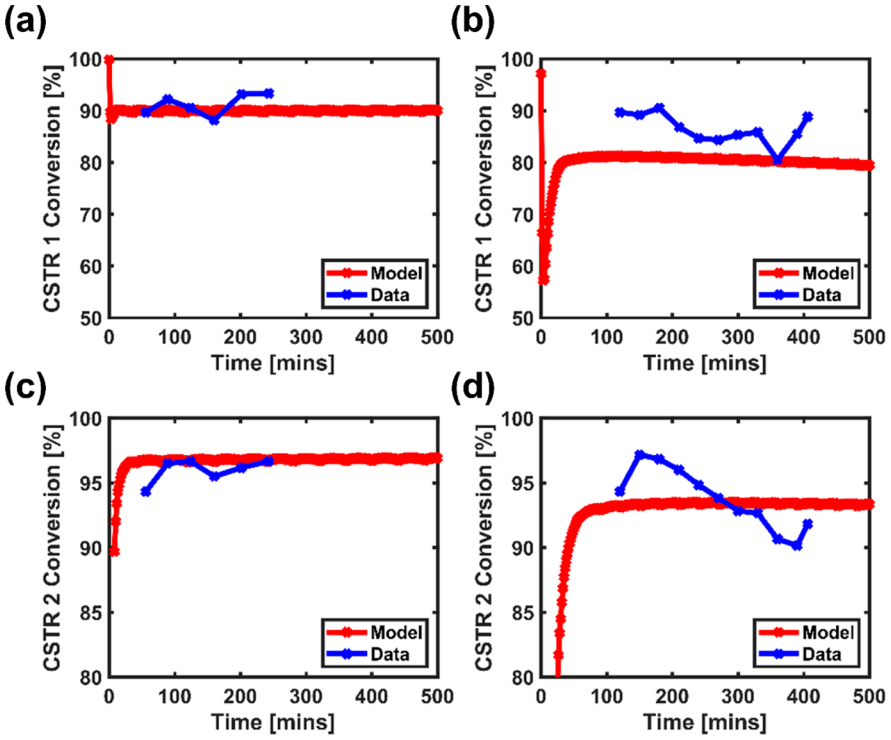

Figure 5. Comparison between model predictions (red) and experimental values (blue) for the kilo-scale demonstration of the Grignard process showing the morpholine amide conversion for (a) CSTR1 at a 40 min Mg dosing interval with a 20 min residence time per reactor at 40 °C, (b) CSTR1 at a 30 min Mg dosing interval with a 30 min residence time per reactor at 30 °C, (c) CSTR2 at a 40 min Mg dosing interval with a 20 min residence time per reactor at 40 °C, and (d) CSTR2 at a 30 min Mg dosing interval with a 30 min residence time per reactor at 30 °C. Each experiment was run following a batch startup in CSTR1, which is why the conversion in CSTR1 dips initially.

Table 3. Range of Measured Morpholine Amide Conversions Observed during Continuous Operation for (1) a 40 min Mg Dosing Interval with a 20 min Residence Time Per Reactor at 40 °C and (2) a 30 min Mg Dosing Interval with a 30 min Residence Time Per Reactor at 30 °C

	conversion range (%)	
case	CSTR1	CSTR2
1	88.2−98.3	94.3−98.5
2	84.3−96.8	92.8−97.2

Following the aqueous quench in CSTR3, the biphasic stream undergoes a liquid−liquid phase separation in decanter 1 (DEC1). The characterization of phase separation and mass transfer kinetics between the aqueous and organic layers was executed in batch experiments. These experiments aimed to characterize the impact of varying the process parameters on the process outcomes such as conversion, partitioning, and mass transfer of all the species between te organic and aqueous layers.

In the experiments to characterize equilibrium partition coefficients, the total solvent content was kept constant, while the compositions of THF, MeTHF, 25 wt % citric acid solution, and methyl *tert*-butyl ether (MTBE) were varied up to ±15% of their nominal values. Additionally, the morpholine amide impurity level was increased up to 3 times its nominal value to reach the specified limit of 95 mol % conversion of morpholine amide, while the morpholine, MgBr·citrate, and enone concentrations were kept at their nominal values. The goal was to show impurity clearance at elevated levels and investigate the effect of concentration on the partition coefficients. The process was shown to be robust and capable of removing elevated impurities. The temperature was also kept at 20 °C. Table 4 summarizes the combinations of

Table 4. Design of Experiments for Characterization of Liquid−Liquid Extraction 1 at 20 °C[a]

	solvent composition (vol %)				concentration			
expt	THF	MeTHF	citric acid	MTBE	product: enone	impurity 1: morpholine amide	impurity 2: morpholine	impurity 3: MgBr·citrate
1	N	N	N	N	1×	3×	1×	1×
2	N + 15%	R	R	R	1×	3×	1×	1×
3	N − 15%	R	R	R	1×	3×	1×	1×
4	R	R	N + 15%	R	1×	3×	1×	1×
5	R	R	N − 15%	R	1×	3×	1×	1×
6	R	R	R	N + 15%	1×	3×	1×	1×
7	R	R	R	N − 15%	1×	3×	1×	1×
8	N	N	N	N	1×	1×	1×	1×

[a]Abbreviations: N, nominal; R, residual; 1×, nominal concentration; 3×, three times elevated morpholine amide impurity concentration.

https://dx.doi.org/10.1021/acs.oprd.0c00188
Org. Process Res. Dev. 2020, 24, 1876−1890

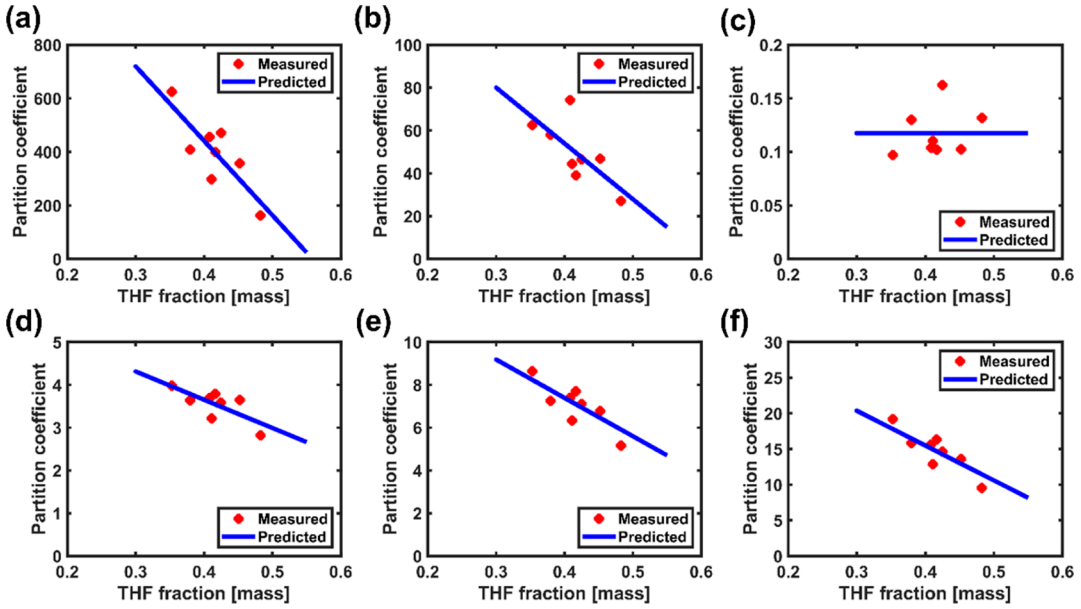

Figure 6. Measured and model-predicted partition coefficients in liquid−liquid extraction 1 for (a) the enone, (b) the morpholine amide, (c) water, (d) THF, (e) MeTHF, and (f) MTBE.

Table 5. Design of Experiments for Characterization of Liquid−Liquid Extraction 2 at 20 °C[a]

	solvent composition					concentration	
expt	THF	MeTHF	citric acid	$NaHCO_3$	MTBE	product: enone	impurity 1: morpholine amide
1	N	N	N	N	N	1×	3×
2	N + 15%	R	R	R	R	1×	3×
3	N − 15%	R	R	R	R	1×	3×
4	R	R	R	N + 15%	R	1×	3×
5	R	R	R	N − 15%	R	1×	3×
6	R	R	R	R	N + 15%	1×	3×
7	R	R	R	R	N − 15%	1×	3×
8	N	N	N	N	N	1×	1×

[a]Abbreviations: N, nominal; R, residual; 1×, nominal concentration; 3×, three times elevated morpholine amide impurity concentration.

conditions used to characterize the equilibrium partition coefficients. The liquid−liquid extraction was allowed to mix for 24 h to allow the phases to reach equilibrium before being analyzed by ultraperformance liquid chromatography (UPLC) for the concentrations of morpholine amide and enone, gas chromatography (GC) for the concentrations of THF, MeTHF, and MTBE, and Karl Fisher (KF) titration for water concentration. The extraction was modeled using the partition coefficient, i.e., the ratio of the concentration of a species in the organic phase to that of the same species in the aqueous phase. As shown in Figure 6, the partition coefficients of the enone, the morpholine amide, THF, MeTHF, and MTBE had a linear dependence on the mass fraction of THF. Also shown in Figure 6 is the lack of dependence of the partition coefficient of water on the mass fraction of THF; the partition coefficient of water was modeled as the average value of all experimental observations. The other species in this extraction, morpholine citrate and magnesium bromide citrate, could not be detected in the organic layer; a partition coefficient of 10^{-3} was assumed for these species.

Mass transfer of all the species (solvents, solutes, and water) present in this step was experimentally confirmed to be much faster than the process time scale (i.e., residence time of <5 min in DEC1) for all studied agitation levels. Therefore, fast mass transfer kinetics was assumed for all of the liquid species as well as the degassing of propene to the reactor headspace.

The reaction of citric acid with sodium bicarbonate to create water, carbon dioxide, and trisodium citrate (eq 17) was considered for CSTR4:

$$3NaHCO_3 + \text{citric acid} \rightarrow \text{trisodium citrate} + 3CO_2 + 3H_2O \quad (17)$$

This reaction was confirmed to be fast under basic reaction conditions, reaching complete conversion in less than 1 min, and was modeled with a rate constant of 10^{-3} $(m^3/mol)^{n-1}$ s^{-1} to have fast acid−base reaction kinetics.

The biphasic reaction stream then undergoes a liquid−liquid phase separation in DEC2. Similar to the acidic workup described above, batch experiments were executed to find partition coefficients for all of the species. For these batch experiments, the total amount of solvent was kept constant, while the compositions of THF, MeTHF, MTBE, citric acid, and sodium bicarbonate solution were varied by up to ±15% of their nominal values. The morpholine amide impurity level was varied up to 3 times the specified limit to reach 95 mol % conversion of morpholine amide, with the enone concentration kept constant at its nominal value. The goal was to show impurity clearance at elevated levels and investigate the effect

https://dx.doi.org/10.1021/acs.oprd.0c00188
Org. Process Res. Dev. 2020, 24, 1876−1890

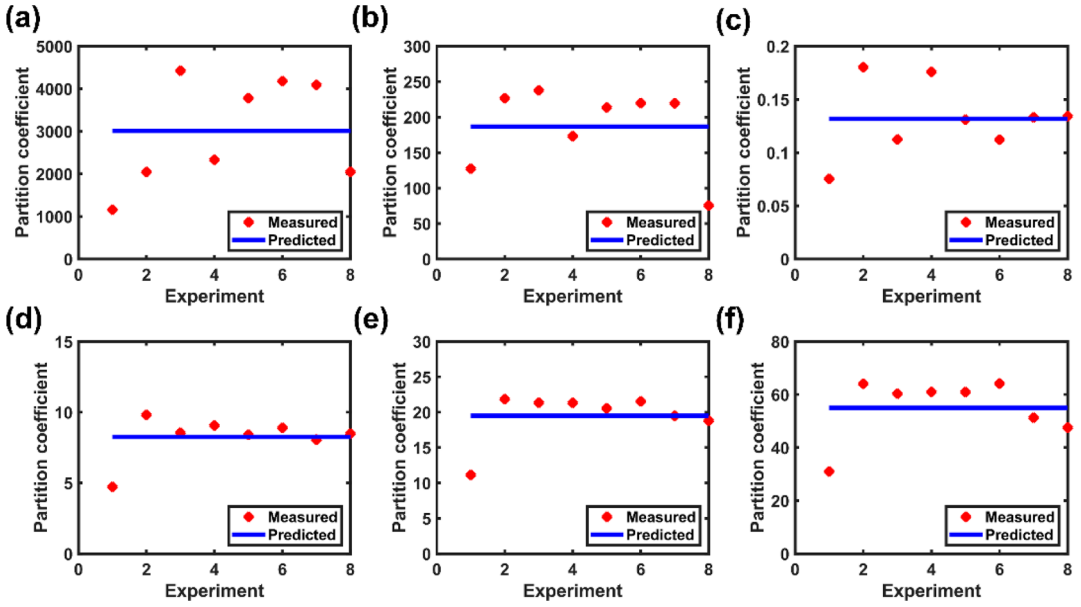

Figure 7. Measured and model-predicted partition coefficients in liquid−liquid extraction 2 for (a) the enone, (b) the morpholine amide, (c) water, (d) MTBE, (e) THF, and (f) MeTHF.

of concentration on the partition coefficients. The process was shown to be robust and capable of removing elevated levels of impurities. The temperature was also kept constant at 20 °C. Table 5 shows all of the combinations of conditions used for partition coefficient characterization. In the liquid−liquid extraction characterization experiments, the phases were allowed to mix for 24 h before being separated and analyzed for the concentrations of morpholine amide **1** and enone **2** by UPLC, THF, MeTHF, and MTBE by GC, and water by KF titration. No strong correlation was identified between the experimental parameters (impurity concentration and solvent and water composition) and the partition coefficient of any species; these coefficients were modeled as the average values of the corresponding experimental observations shown in Figure 7. The only species not detected in the organic phase, trisodium citrate, was modeled with a partition coefficient of 10^{-3}.

Mass transfer of all the species (solvents, solutes, and water) in DEC2 was experimentally confirmed to be fast relative to the process time scale (i.e., a residence time of <5 min in DEC2). No mixing sensitivity was observed for mass transfer at any of the studied agitation levels. Therefore, fast mass transfer kinetics was assumed for all of the species. Carbon dioxide was assumed to be transferred to the reactor headspace at a high mass transfer rate.

2.3. Distillation Model Development. The final unit operation, a distillation drum, serves to swap the enone solvent from MeTHF, THF, and MTBE to a combination of acetonitrile and acetic acid. Specifically, the process is designed to achieve ≤0.5 wt % each of MeTHF, THF, and MTBE and 25 wt % enone such that the epoxidation reaction in the third synthesis step of the overall process can be performed efficiently in acetonitrile. The distillation process is semibatch and constrained to have a maximum internal temperature of 40 °C and a vacuum pressure of <200 mbar. Once the hold tank reaches a specified volume, a fixed volume of process solution is charged to the distillation drum. The mixture in the distillation drum is then distilled to a specified volume, to which acetonitrile is charged and the resulting new mixture is distilled again to a specified volume. The charge and distillation volumes for these steps were determined with the DynoChem solvent swap distillation model and then verified experimentally on the development scale. After completion of the final distillation step, the product solution is diluted with acetic acid and transferred to the product collection tank, which is sent downstream to the third synthesis step of the epoxy ketone manufacturing process. This semibatch distillation is repeated continuously to provide a steady feed to the next synthesis step.

In the virtual plant flowsheet, the gPROMS FormulatedProducts distillation drum model was used in conjunction with its Task functionality to describe the operating procedure. The vapor−liquid equilibrium was modeled using temperature-dependent two-liquid binary interaction parameters from the nonrandom two-liquid (NRTL) model for MeTHF, THF, MTBE, ACN, and water.[24] Fast mass transfer of the solvents and water between the liquid and vapor phases was assumed, with the overall volumetric mass transfer coefficient modeled as 1 s^{-1}. The enone and any impurities were treated as nonvolatile species.

2.4. Computational Methods. The end-to-end simulation was created in gPROMS FormulatedProducts version 1.4 from Process Systems Enterprise.[25] A database containing physical and thermodynamic properties of proprietary and other compounds was developed using gPROMS FormulatedProducts Utilities and MultiFlash 6.1. NRTL activity coefficients describing the vapor−liquid equilibria of water and solvents were obtained from Dechema.[24] All of the unit operations, including CSTRs, decanters, and the distillation drum, were modeled with gPROMS FormulatedProducts standard and custom library models. The semibatch distillation drum operation was modeled using the gPROMS FormulatedProducts Task, a feature of this modeling software that enables hybrid continuous−discrete modeling.[26]

Kinetic parameter estimates for reactions occurring in CSTR1 and CSTR2 were determined in gPROMS using concentration measurements for both the reactant and product. The reactions occurring in CSTR3 and CSTR4

https://dx.doi.org/10.1021/acs.oprd.0c00188
Org. Process Res. Dev. 2020, 24, 1876−1890

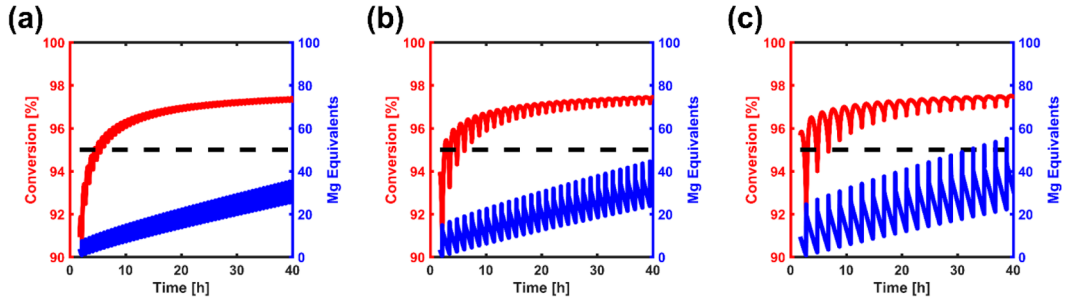

Figure 8. Number of Mg equivalents in CSTR1 (blue) and morpholine amide conversion in CSTR2 (red) for magnesium dosing intervals of (a) 40 min, (b) 80 min, and (c) 120 min. The black dashed lines show the target morpholine amide conversion (95%).

were confirmed to follow fast acid−base kinetics and therefore were not calibrated. The partition coefficients for the liquid−liquid equilibrium in DEC1 had a linear dependence on the total THF mass fraction and were modeled as such. The partition coefficients for the liquid−liquid equilibrium in DEC2 were modeled as the average values from all experimental data. The mass transfer coefficients for the liquid−liquid equilibria in DEC1 and DEC2 were confirmed to be sufficiently large and were not estimated. For the distillation drum, the mass transfer coefficients were assumed to be large and therefore were not characterized.

For level control within each relevant unit operation, the outflow condition was based on a fixed-volume specification. For temperature control, an embedded model was used to manipulate the temperature of the incoming heat transfer fluid. The heat transfer coefficients for glass reactors were estimated to be 4.56 W/K using DynoChem Utilities.[27]

For disturbance analysis, the simulation was first run with nominal conditions to reach steady state (10 000 s), unless otherwise specified. Following the simulation under nominal conditions, disturbances were introduced as step changes and allowed to reach steady state. Process disturbances were determined on the basis of expected fluctuations at scale, and model disturbances were determined on the basis of either (1) the standard deviations of the determined parameters or (2) the largest difference between the model predictions and experimental data in the calibration set.

3. RESULTS AND DISCUSSION

After individual calibration, the models were connected in a flowsheet-level integrated model including regulatory control loops for dynamic simulation. The integrated model for the overall Step 2 process was then used to determine (1) the relationship among the magnesium charging interval, average number of magnesium equivalents in the reaction, and the morpholine amide conversion and (2) the impact of process disturbances and uncertainties on various CQAs. These analyses were used to guide operational decisions and the development of a process control strategy.

3.1. Case Study for the Development of an Operation Strategy: Mg Charging Strategy. The development of a Mg charging strategy is a crucial step in continuous Grignard reactions to maximize the time between Mg charges but minimize variability in the reactor conditions, including the number of Mg equivalents and the reaction conversion. For development runs, the Mg charging interval was kept low[19] at 30−40 min to maintain process stability. Instead of performing additional highly complex development runs, the validated Grignard reaction model was used to understand the

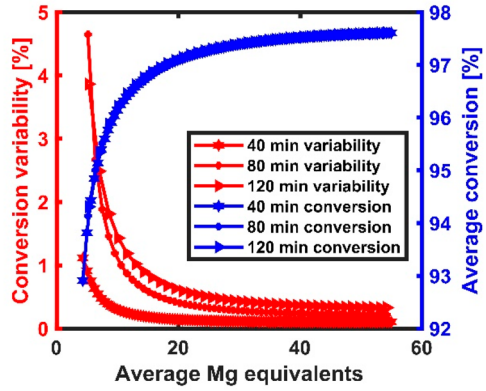

Figure 9. Variability in morpholine amide conversion leaving CSTR2 as a function of average number of magnesium equivalents in CSTR1 and magnesium dosing interval (40, 80, or 120 min) (red) and average morpholine amide conversion leaving CSTR2 as a function of those same parameters (blue).

relationship between operational tractability (i.e., frequency of manual magnesium dosing) and process stability (i.e., consistency of enone conversion).

The use of in silico modeling was critical for this analysis since experimental characterization of the full design space for this reaction was difficult because of (1) the lack of accurate methods to measure the number of Mg equivalents in real time and (2) the variability in CSTR conversion due to the noncontinuous nature of the magnesium dosing. The objective of the in silico studies was to investigate the range of morpholine amide conversions for a given range of magnesium equivalents. Figure 8 shows the morpholine amide conversion as a function of the total number of Mg equivalents in CSTR1 for three different dosing strategies (40, 80, and 120 min). In the simulation, the reaction is assumed to have been initiated with a very small amount of Mg, in contrast to the normal batch initiation with a greater amount of Mg. Then magnesium is dosed in each interval such that the number of magnesium equivalents gradually increases over time. At earlier times in the simulation, the number of magnesium equivalents is quite low (~5), and therefore, the variability in conversion is quite high. As the number of magnesium equivalents increases, both the variability and the average conversion asymptotically approach constant values. The inflection point for this variability is around 12 magnesium equivalents, in agreement with batch characterization heuristics that suggested operation at a minimum of 12 magnesium equivalents to achieve the 95% conversion target. These trends are consistent with the underlying chemistry: at a greater number of magnesium

https://dx.doi.org/10.1021/acs.oprd.0c00188
Org. Process Res. Dev. 2020, 24, 1876−1890

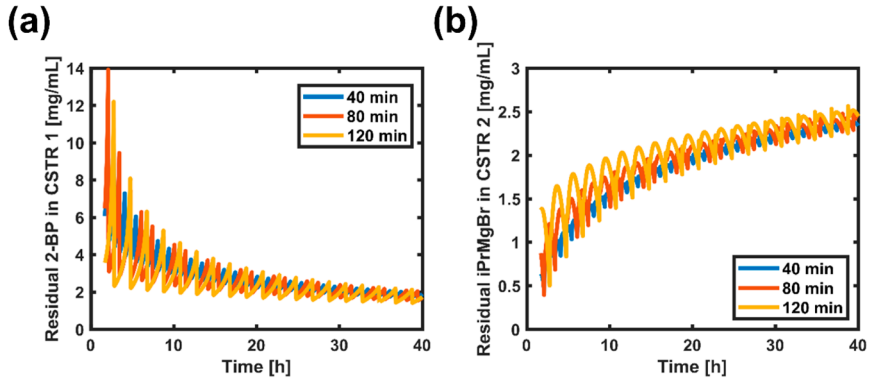

Figure 10. Impact of the dosing interval (40, 80, or 120 min) on the residual concentrations of (a) 2-BP in CSTR1 and (b) isopropenylmagnesium bromide in CSTR2.

Table 6. Process Uncertainties in the Form of Operational Disturbances Considered in the Disturbance Analyses

stream or unit	variable	allowed tolerance
morpholine amide solution in THF/MeTHF	flow rate	±10% of total flow rate
morpholine amide solution in THF/MeTHF	molarity of morpholine amide	±10% of total molarity
2-BP solution in THF	flow rate	±10% of total flow rate
2-BP solution in THF	molarity of 2-BP	±10% of total molarity
25 wt % aq citric acid solution	flow rate	±10% of total flow rate
25 wt % aq citric acid solution	weight percent of citric acid	±10% of total weight fraction
MTBE	flow rate	±10% of total flow rate
8 wt % $NaHCO_3$	flow rate	±10% of total flow rate
8 wt % $NaHCO_3$	weight fraction of $NaHCO_3$	±10% of total weight fraction
CSTR1	temperature	±5 °C
CSTR1	fill level	±10% Reactor volume
CSTR2	temperature	±5 °C
CSTR2	fill level	±10% of reactor volume
CSTR3	fill level	±10% of reactor volume
CSTR4	fill level	±10% of reactor volume

Table 7. Model Uncertainties in the Form of Parametric Uncertainties Considered in the Disturbance Analyses

stream or unit	variable	allowed tolerance
CSTR1/CSTR2	forward reaction rate (eq 1)	±10% of absolute value
CSTR1/CSTR2	forward reaction rate (eq 11)	±10% of absolute value
CSTR1/CSTR2	forward reaction rate (eq 12)	±10% of absolute value
DEC1	imidazole partition coefficient	±10% of absolute value
DEC1	morpholine partition coefficient	±10% of absolute value
DEC1	imidazole-HCl partition coefficient	±10% of absolute value
DEC1	morpholine amide partition coefficient	+28/−33% of absolute value
DEC1	water partition coefficient	+18/−11% of absolute value
DEC1	MeTHF partition coefficient	+12/−17% of absolute value
DEC1	HCl partition coefficient	+18/−11% of absolute value
DEC2	Boc-Leu-OH partition coefficient	±10% of absolute value
DEC2	morpholine amide partition coefficient	+21/−25% of absolute value
DEC2	water partition coefficient	+36/−43% of absolute value
DEC2	MeTHF partition coefficient	+12/−43% of absolute value
DEC2	Na_2CO_3 partition coefficient	+36/−43% of absolute value
DEC2	NaCl partition coefficient	±10% of absolute value
DEC2	$NaHCO_3$ partition coefficient	±10% of absolute value
DEC2	HCl partition coefficient	±10% of absolute value

equivalents, each magnesium charge causes a smaller relative change in the magnesium surface concentration, resulting in a smaller relative change in morpholine amide conversion. In Figure 9, this analysis is then used to determine the variability in average morpholine amide conversion as a function of dosing interval and average number of magnesium equivalents. Interestingly, at a fixed number of magnesium equivalents, the conversion variability increases with increasing dosing time, but the average morpholine amide conversion remains relatively constant. Additionally, as the average number of magnesium equivalents increases, the variabilities for all cases asymptotically approach a minimum value for each dosing interval. Both trends make qualitative sense, but there is likely some upper limit on the number of magnesium equivalents in CSTR1 that has not been characterized. This analysis can then be used to determine the maximum dosing interval (i.e., the least complex process) from a desired variability in morpholine amide conversion (i.e., the most stable process). Furthermore, once the conversion variability and the corresponding dosing interval have been identified, the measured variability in conversion can be used as a soft sensor for the average number of magnesium equivalents in the reactor. Having this measurement is critical, as stirred tanks are integrated systems and thus are difficult to control without feedback from real-time measurements.

While quantifying the variability in conversion of the main reactant is important, understanding how this variability impacts the impurity profile is critical for the development of a robust process. Figure 10 shows the residual concentrations of 2-BP and isopropenylmagnesium bromide in CSTR2 over time for three different magnesium charging intervals. Downstream of CSTR2, 2-BP is removed in the distillation

https://dx.doi.org/10.1021/acs.oprd.0c00188
Org. Process Res. Dev. 2020, 24, 1876−1890

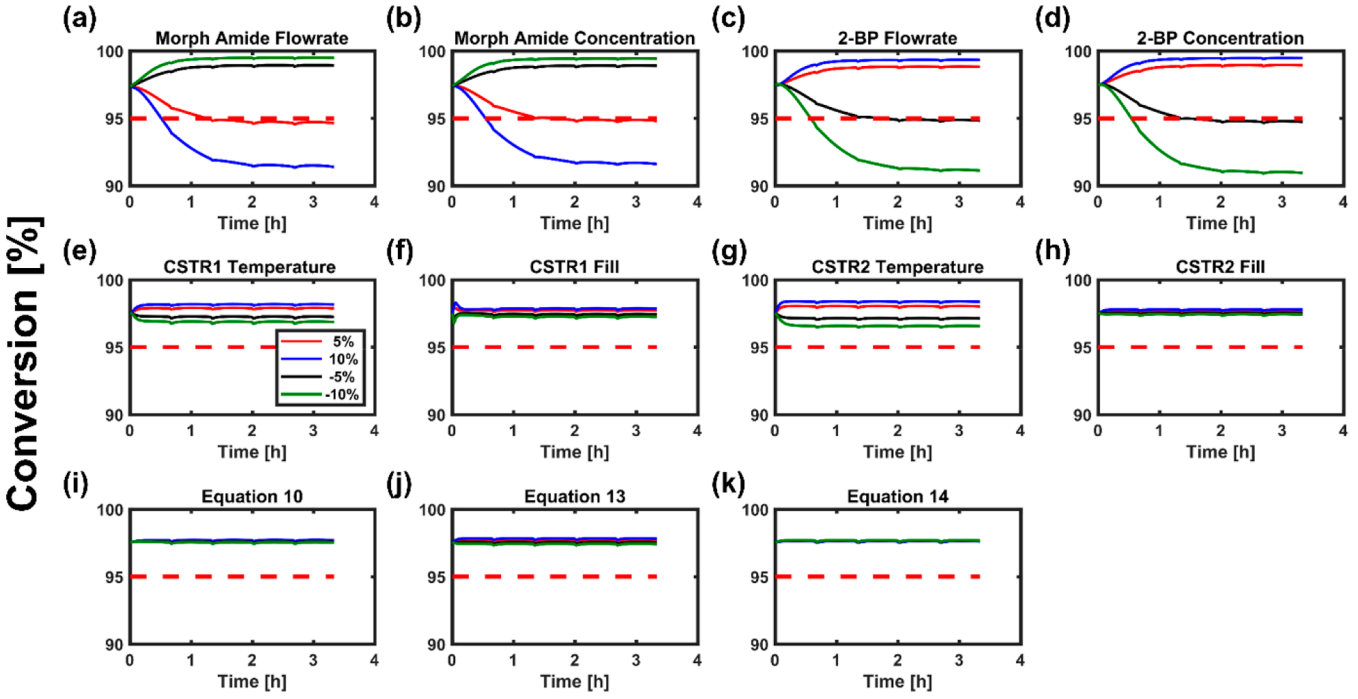

Figure 11. Conversion of morpholine amide as a function of (a) morpholine amide flow rate, (b) morpholine amide concentration, (c) 2-BP flow rate, (d) 2-BP concentration, (e) CSTR1 temperature, (f) CSTR1 fill level, (g) CSTR2 temperature, (h) CSTR2 fill level (i) eq 10 rate constant ($k_r C^*_{Mg}$), (j) eq 13 rate constant, and (k) eq 14 rate constant. The legend in (e) is the same as in the rest of the figure, and the bounds correlate to the maximum (+10%), minimum (−10%), half-maximum (+5%), and half-minimum (−5%) of the values in Tables 6 and 7.

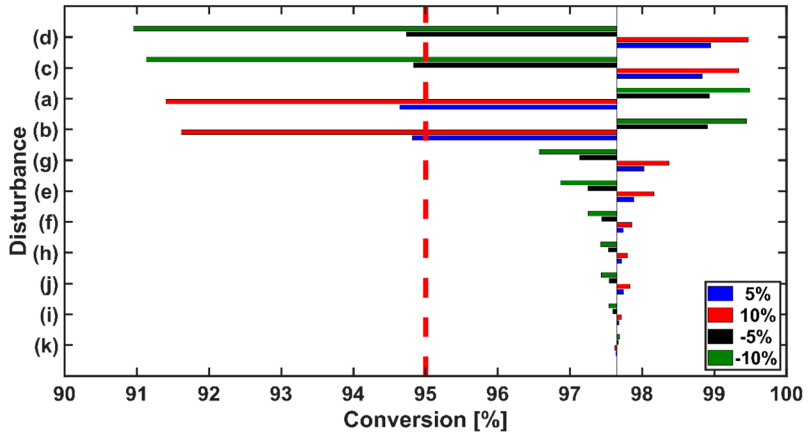

Figure 12. Tornado diagram for the conversion of morpholine amide as a function of (a) morpholine amide flow rate, (b) morpholine amide concentration, (c) 2-BP flow rate, (d) 2-BP concentration, (e) CSTR1 temperature, (f) CSTR1 fill level, (g) CSTR2 temperature, (h) CSTR2 fill level (i) eq 10 rate constant ($k_r C^*_{Mg}$), (j) eq 13 rate constant, and (k) eq 14 rate constant.

drum because of its volatility, and isopropenylmagnesium bromide is removed in CSTR3 upon the addition of citric acid to quench the tetrahedral intermediate. Understanding how these charging strategies can impact the residual concentrations provides insight into the amount of overdesign required for the quench reaction. As the number of magnesium equivalents increases, the residual concentration of 2-BP decreases and the residual concentration of isopropenylmagnesium bromide increases. However, the variability in the isopropenylmagnesium bromide concentration does not exceed the experimentally characterized range and can be removed in downstream operations.

Taken together, the simulation results indicate that the process could be made less operationally complex by reducing the Mg charging interval and increasing the residual number of magnesium equivalents. On the basis of in silico process development studies, a residence time of 40 min and a minimum of 12 equiv of Mg were recommended as operating parameters. Implementation of this approach would result in a process that delivers the CQAs and maintains a relatively stable impurity profile.

3.2. Process Disturbance Analysis. After identification of the Mg charge strategy, the flowsheet-level integrated dynamic model was used to determine how disturbances and uncertainties would impact various CQAs. All of the process specifications were initially developed for the batch process and targeted by the continuous process. The uncertainties studied in this paper belong to two groups: process

https://dx.doi.org/10.1021/acs.oprd.0c00188
Org. Process Res. Dev. 2020, 24, 1876−1890

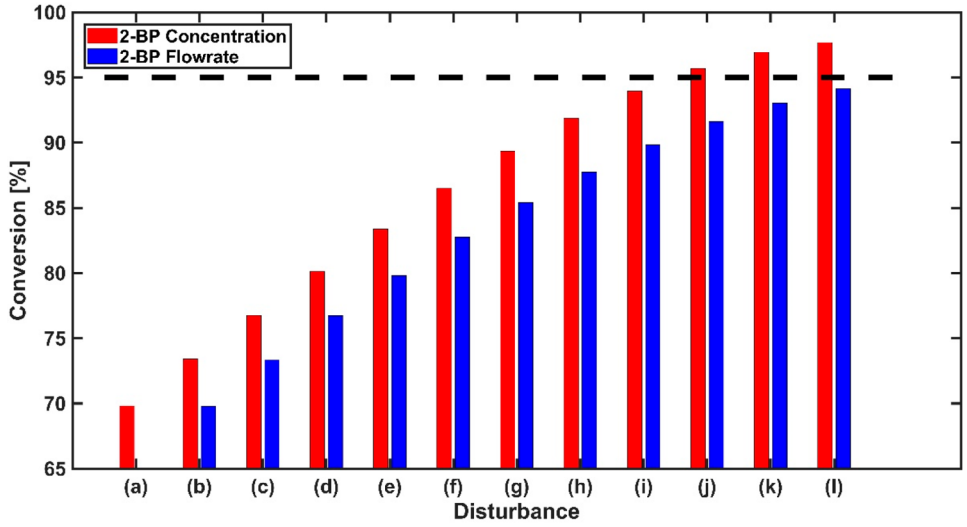

Figure 13. Reduction and recovery in the conversion of morpholine amide leaving CSTR2 for (a) the worst-case scenario of operating conditions, (b) decreased 2-BP concentration/flow rate (−5% of nominal), (c) nominal 2-BP concentration/flow rate, (d) increased 2-BP concentration/flow rate (+5% of nominal), (e) increased 2-BP concentration/flow rate (+10% of nominal), (f) increased 2-BP concentration/flow rate (+15% of nominal), (g) increased 2-BP concentration/flow rate (+20% of nominal), (h) increased 2-BP concentration/flow rate (+25% of nominal), (i) increased 2-BP concentration/flow rate (+30% of nominal), (j) increased 2-BP concentration/flow rate (+35% of nominal), (k) increased 2-BP concentration/flow rate (+40% of nominal), and (l) increased 2-BP concentration/flow rate (+45% of nominal).

uncertainties and model uncertainties. Process uncertainties consist of operational disturbances, including flow rates and concentrations of feed streams, temperatures, and fill levels of unit operations, and are shown in Table 6. Model uncertainties consist of parametric uncertainties of estimated kinetic and thermodynamic parameters and are shown in Table 7. All of the CPPs were recorded in the simulation, but the major focus of this analysis is the conversion of morpholine amide leaving CSTR2. To decouple these effects from the magnesium charging interval, the number of magnesium equivalents was kept very high (∼30) to minimize variability due to residual magnesium levels.

The step response matrices for the conversion of morpholine amide leaving CSTR2 are shown in Figure 11. In this figure, oscillations at steady state are due to each magnesium charge. As shown, operational disturbances in the morpholine amide flow rate, morpholine amide concentration, 2-BP flow rate, and 2-BP concentration have a strong impact on the conversion, while operational disturbances in the CSTR1 temperature, CSTR1 fill level, CSTR2 temperature, and CSTR2 fill level and model uncertainties in kinetic parameter estimates have a moderate impact on the conversion. All of the other disturbances and uncertainties have negligible impacts on the conversion of CSTR2 and are not shown.

The total impact and relative magnitudes of impact of these disturbances and uncertainties are illustrated in a tornado diagram (Figure 12). As expected, larger changes in conversion are caused by operational disturbances that change the amounts of supplied reactants. This occurs because the reactants are supplied at nearly stoichiometric amounts—the residual concentration of isopropenylmagnesium bromide, the excess reactant, is 20 mM. The other disturbances impact the relative reaction rate but are still limited by the reaction equivalents.

In terms of developing a robust process, the conversion does not meet the desired minimum conversion of 95% for some operational disturbance scenarios. Additionally, the worst-case scenario for all uncertainties combined can result in conversions as low as 70%. It would be a highly unlikely scenario to have all of the worst-case disturbances and uncertainties occur simultaneously. Even in this unlikely scenario, a design change or feedback control in the form of changing a process variable can recover the process to meet the target conversion of 95%. In terms of design, in silico analysis demonstrates that a 35% increase in 2-BP concentration is required to maintain the target-level process specifications for the worst-case combination of all disturbances. In terms of control, it is preferred to manipulate process variables with a strong impact on conversion. However, it is not practical to manipulate two of these variables, the concentration and flow rate of incoming morpholine amide, because this stream is produced upstream in the continuous manufacturing process. This leaves three options for manipulated variables: (1) the temperature of CSTR1, (2) the temperature of CSTR2, and (3) the flow rate of 2-BP. Since the Grignard reaction is a highly exothermic reaction, controlling the temperatures of CSTR1 and CSTR2 is not desirable because of process safety impacts. Therefore, the flow rate of 2-BP was selected as a desirable manipulated variable to control the reaction conversion. As shown in Figure 13, the conversion monotonically increases with 2-BP flow rate for the combination of worst-case disturbances, suggests that this would be a suitable manipulated variable. This control strategy was not implemented in order to reduce the complexity associated with adjusting the Mg charges in real time during production in accordance with changes in 2-BP flow rate for sufficient Grignard reagent generation. Instead, strict regulatory control specifications were defined on key operational parameters of the process to minimize disturbances. This includes implementing flow rate control and concentration specifications on critical reagent streams and reaction temperature control with narrow qualified ranges.

https://dx.doi.org/10.1021/acs.oprd.0c00188
Org. Process Res. Dev. 2020, 24, 1876−1890

CONCLUSIONS

This paper has described the development of a virtual plant to characterize and build a robust process control strategy for the preparation of enone **2** by an integrated continuous process consisting of seven unit operations, including a highly exothermic Barbier-type Grignard reaction. Individual unit operation models were developed on the basis of mechanistic understanding and targeted data-rich experiments, and process predictions were validated at the development scale. Model agreement was generally acceptable: the conversion of morpholine amide varied from 94.3% to 98.5% compared to 97.9% predicted by the model. The models developed for the individual unit operations were connected in an end-to-end integrated flowsheet model, which was used to simulate the continuous manufacturing process for enone **2**. The simulations included various Mg charging strategies as well as an assessment of the impact of process disturbances on the operational performance and product quality. The process was found to be sensitive to operational disturbances in the supplied reactants, with process design and operation strategies focusing on the concentration and flow rate of the 2-BP supply stream to CSTR1. These analyses allowed for the development of advanced control strategies for the CM process.

AUTHOR INFORMATION

Corresponding Author

Elçin Içten − *Process Development, Amgen, Inc., Cambridge, Massachusetts 02142, United States;* orcid.org/0000-0002-0962-7550; Email: eicten@amgen.com

Authors

Andrew J. Maloney − *Department of Chemical Engineering, Massachusetts Institute of Technology, Cambridge, Massachusetts 02139, United States;* orcid.org/0000-0002-9744-6433

Matthew G. Beaver − *Process Development, Amgen, Inc., Cambridge, Massachusetts 02142, United States;* orcid.org/0000-0003-3816-4601

Xiaoxiang Zhu − *Process Development, Amgen, Inc., Cambridge, Massachusetts 02142, United States*

Dongying E. Shen − *Process Development, Amgen, Inc., Cambridge, Massachusetts 02142, United States*

Jo Anna Robinson − *Process Development, Amgen, Inc., Cambridge, Massachusetts 02142, United States*

Andrew T. Parsons − *Process Development, Amgen, Inc., Cambridge, Massachusetts 02142, United States;* orcid.org/0000-0002-0320-0919

Ayman Allian − *Process Development, Amgen, Inc., Thousand Oaks, California 91320, United States*

Seth Huggins − *Process Development, Amgen, Inc., Thousand Oaks, California 91320, United States*

Roger Hart − *Process Development, Amgen, Inc., Cambridge, Massachusetts 02142, United States*

Pablo Rolandi − *Process Development, Amgen, Inc., Cambridge, Massachusetts 02142, United States*

Shawn D. Walker − *Process Development, Amgen, Inc., Cambridge, Massachusetts 02142, United States;* orcid.org/0000-0001-8827-4679

Richard D. Braatz − *Department of Chemical Engineering, Massachusetts Institute of Technology, Cambridge, Massachusetts 02139, United States;* orcid.org/0000-0003-4304-3484

Complete contact information is available at: https://pubs.acs.org/10.1021/acs.oprd.0c00188

Notes

The authors declare no competing financial interest.

ACKNOWLEDGMENTS

The authors acknowledge Gerard Capellades Mendez from MIT for the scientific discussions and Silei Xiong, Amit Goda, Meera Mahadevan, Ananya Chowdhury, and Kevin Healy from Process Systems Enterprise Ltd. for their support on gPROMS models. The contribution of A.J.M. was partially supported by the National Science Foundation Graduate Research Fellowship under Grant 1122374. Any opinion, findings, and conclusions or recommendations expressed in this material are those of the authors(s) and do not necessarily reflect the views of the National Science Foundation.

ABBREVIATIONS

2-BP, 2-bromopropene; ACN, acetonitrile; AcOH, acetic acid; CM, continuous manufacturing; CPP, critical process parameter; CQA, critical quality attribute; CSTR, continuously stirred tank reactor; DEC, decanter; FTIR, Fourier transform infrared spectroscopy; GC, gas chromatography; HPLC, high-performance liquid chromatography; IPC, in-process control; KF, Karl Fischer; LLE, liquid−liquid extraction; MeTHF, 2-methyltetrahydrofuran; Mg, magnesium; MTBE, methyl *tert*-butyl ether; PAT, process analytical technology; QbC, quality by control; QbD, quality by design; SSQ, sum of squares; UPLC, ultraperformance liquid chromatography

REFERENCES

(1) Su, Q.; Ganesh, S.; Moreno, M.; Bommireddy, Y.; Gonzalez, M.; Reklaitis, G. V.; Nagy, Z. K. A Perspective on Quality-by-Control (QbC) in Pharmaceutical Continuous Manufacturing. *Comput. Chem. Eng.* **2019**, *125*, 216−231.

(2) Cole, K. P.; Groh, J. M.; Johnson, M. D.; Burcham, C. L.; Campbell, B. M.; Diseroad, W. D.; Heller, M. R.; Howell, J. R.; Kallman, N. J.; Koenig, T. M.; et al. Kilogram-Scale Prexasertib Monolactate Monohydrate Synthesis under Continuous-Flow CGMP Conditions. *Science* **2017**, *356* (6343), 1144−1150.

(3) Lee, S. L.; O'Connor, T. F.; Yang, X.; Cruz, C. N.; Chatterjee, S.; Madurawe, R. D.; Moore, C. M. V.; Yu, L. X.; Woodcock, J. Modernizing Pharmaceutical Manufacturing: From Batch to Continuous Production. *J. Pharm. Innovation* **2015**, *10*, 191−199.

(4) Icten, E.; Maloney, A. J.; Beaver, M. G.; Shen, D. E.; Zhu, X.; Graham, L. R.; Robinson, J. A.; Huggins, S.; Allian, A. D.; Hart, R.; et al. A Virtual Plant for Integrated Continuous Manufacturing of a Carfilzomib Drug Substance Intermediate, Part 1: CDI-Promoted Amide Bond Formation. *Org. Process Res. Dev.* **2020**, DOI: 10.1021/acs.oprd.0c00187.

(5) Myerson, A. S.; Krumme, M.; Nasr, M.; Thomas, H.; Braatz, R. D. Control Systems Engineering in Continuous Pharmaceutical Manufacturing May 20−21, 2014 Continuous Manufacturing Symposium. *J. Pharm. Sci.* **2015**, *104* (3), 832−839.

(6) Reklaitis, G. V. Prospects and Challenges for Process Systems Engineering in Healthcare. *Comput. Aided Chem. Eng.* **2017**, *40*, 3−7.

(7) Hirshfield, L.; Içten, E.; Giridhar, A.; Nagy, Z. K.; Reklaitis, G. V. Real-Time Process Management Strategy for Dropwise Additive Manufacturing of Pharmaceutical Products. *J. Pharm. Innovation* **2015**, *10* (2), 140−155.

(8) Içten, E.; Reklaitis, G. V.; Nagy, Z. K. Advanced Control for the Continuous Dropwise Additive Manufacturing of Pharmaceutical Products. *Comput. Aided Chem. Eng.* **2018**, *41*, 379−401.

(9) Benyahia, B.; Lakerveld, R.; Barton, P. I. A Plant-Wide Dynamic Model of a Continuous Pharmaceutical Process. *Ind. Eng. Chem. Res.* **2012**, *51* (47), 15393−15412.
(10) Lakerveld, R.; Benyahia, B.; Braatz, R. D.; Barton, P. I. Model-Based Design of a Plant-Wide Control Strategy for a Continuous Pharmaceutical Plant. *AIChE J.* **2013**, *59* (10), 3671−3685.
(11) Lakerveld, R.; Benyahia, B.; Heider, P. L.; Zhang, H.; Wolfe, A.; Testa, C. J.; Ogden, S.; Hersey, D. R.; Mascia, S.; Evans, J. M. B.; et al. The Application of an Automated Control Strategy for an Integrated Continuous Pharmaceutical Pilot Plant. *Org. Process Res. Dev.* **2015**, *19* (9), 1088−1100.
(12) Ierapetritou, M.; Escotet-Espinoza, M. S.; Singh, R. Process Simulation and Control for Continuous Pharmaceutical Manufacturing of Solid Drug Products. In *Continuous Manufacturing of Pharmaceuticals*; Kleinebudde, P., Khinast, J., Rantanen, J., Eds.; Wiley, 2017; Chapter 2, pp 33−105.
(13) Içten, E.; Nagy, Z. K.; Reklaitis, G. V. Process Control of a Dropwise Additive Manufacturing System for Pharmaceuticals Using Polynomial Chaos Expansion Based Surrogate Model. *Comput. Chem. Eng.* **2015**, *83*, 221−231.
(14) Içten, E.; Giridhar, A.; Taylor, L. S.; Nagy, Z. K.; Reklaitis, G. V. Dropwise Additive Manufacturing of Pharmaceutical Products for Melt-Based Dosage Forms. *J. Pharm. Sci.* **2015**, *104* (5), 1641−1649.
(15) *PD2M Future of Pharmaceutical Manufacturing Workshop*. AICHE Pharmaceutical Discovery Development and Manufacturing Forum (PD2M), November 2019. https://www.aiche.org/conferences/future-pharmaceutical-manufacturing-workshop/2019 (accessed 2020-04-15).
(16) Rakita, P. E. Safe Handling Practices of Industrial Scale Grignard Reagents. In *Handbook of Grignard Reagents*; Silverman, G. S., Rakita, P. E., Eds.; CRC Press, 1996; Chapter 5, pp 79−88.
(17) Kopach, M. E.; Roberts, D. J.; Johnson, M. D.; McClary Groh, J.; Adler, J. J.; Schafer, J. P.; Kobierski, E.; Trankle, W. G. The Continuous Flow Barbier Reaction: An Improved Environmental Alternative to the Grignard Reaction? *Green Chem.* **2012**, *14* (5), 1524−1536.
(18) Dornan, P.; Anthoine, T.; Beaver, M.; Cheng, G. C.; Cohen, D.; Cui, S.; Lake, W.; Langille, N.; Lucas, S.; Patel, J.; et al. Continuous Process Improvement in the Manufacture of Carfilzomib, Part 1: Process Understanding and Improvements in the Commercial Route to Prepare the Epoxyketone Warhead. *Org. Process Res. Dev.* **2020**, *24* (4), 481−489.
(19) Beaver, M.; Shi, X.; Riedel, J.; Patel, P.; Zeng, A.; Corbett, M.; Robinson, J. A.; Parsons, A.; Cui, S.; Baucom, K.; et al. Continuous Process Improvement in the Manufacture of Carfilzomib, Part 2: An Improved Process for Synthesis of the Epoxyketone Warhead. *Org. Process Res. Dev.* **2020**, *24* (4), 490−499.
(20) Changi, S. M.; Wong, S. Kinetics Model for Designing Grignard Reactions in Batch or Flow Operations. *Org. Process Res. Dev.* **2016**, *20* (2), 525−539.
(21) Wong, S.; Changi, S. M.; Shields, R.; Bell, W.; Mcgarvey, B.; Johnson, M. D.; Sun, W.; Braden, T. M.; Kopach, M. E.; Spencer, R. D.; et al. Operation Strategy Development for Grignard Reaction in a Continuous Stirred Tank Reactor. *Org. Process Res. Dev.* **2016**, *20* (2), 540−550.
(22) Maloney, A. J.; Icten, E.; Capellades, G.; Beaver, M. G.; Zhu, X.; Graham, L.; Brown, D. B.; Griffin, D. J.; Sangodkar, R.; Allian, A.; et al. A Virtual Plant for Integrated Continuous Manufacturing of a Carfilzomib Drug Substance Intermediate, Part 3: Manganese-Catalyzed Asymmetric Epoxidation, Crystallization, and Filtration. *Org. Process Res. Dev.* **2020**, DOI: 10.1021/acs.oprd.0c00189.
(23) Peltzer, R. M.; Eisenstein, O.; Nova, A.; Cascella, M. How Solvent Dynamics Controls the Schlenk Equilibrium of Grignard Reagents: A Computational Study of CH_3MgCl in Tetrahydrofuran. *J. Phys. Chem. B* **2017**, *121* (16), 4226−4237.
(24) *Dechema Chemistry Data Series, Vol. 1*; Deutsche Gesellschaft fur Chemisches Aparatewesen, 2004.
(25) Process Systems Enterprise. *gPROMS FormulatedProducts*. https://www.psenterprise.com/products/gproms/formulatedproducts (accessed 2020-04-15).
(26) Barton, P. I.; Pantelides, C. C. Modeling of Combined Discrete/Continuous Processes. *AIChE J.* **1994**, *40* (6), 966−979.
(27) *DynoChem Resources*. https://dcresources.scale-up.com (accessed 2020-04-15).

https://dx.doi.org/10.1021/acs.oprd.0c00188
Org. Process Res. Dev. 2020, 24, 1876−1890